

Solution processed Ag–In–S nanoparticles as light adsorber in ZnO for photovoltaic application

K. Abinaya¹, P. Sharvanti², N. Rajeswari Yogamalar^{3,a}

¹London South Bank University, London, UK

²Research and Development, Saint Gobain, San Diego, California, USA

³Hindustan Institute of Technology and Science, Padur, Kelambakkam, Chennai, India

^arajeswariyogamalar.n@gmail.com

Corresponding author: N. Rajeswari Yogamalar, rajeswariyogamalar.n@gmail.com

ABSTRACT Nano-sized indium incorporated silver sulphide (Ag–In–S) nanocomposites were synthesized by simple wet chemical method as an electron transport layer in zinc oxide (ZnO) for high efficient photovoltaic (PV) cell. The inclusion of high conductivity indium ions in Ag₂S will improve the facile electron transfer and the assembled hetero-structure features the solar light harvesting in PV cell. The powder X-ray diffraction (XRD) studies confirmed the formation of indium incorporated Ag₂S (A/IS) nanocomposites and ZnO/AIS (ZAIS) compound nanocomposites crystallizing in pure monoclinic phase and mixed wurtzite hexagonal, monoclinic and tertiary phases respectively. The wide particle size distributions in ZAIS clearly revealed the adherence of AIS nanocomposites in ZnO lattice thus, promoting the light adsorption property. In addition, the tuning of the optical bandgap covering the entire solar spectrum (UV, visible, and infra-red regions), multiple-band electron transitions and hence, promoting the fast electron transportation are effectively achieved in ZAIS compound nanocomposites. With this simple positive approach, the PV cell efficiency is pushed forward with the In³⁺ metal ion incorporation however; enhanced, enriched solar cell efficiency can be later tuned up with the detailed optimization studies.

KEYWORDS Electron transport layer, nanocomposites, hetero-structure, nano-confinement, light adsorption.

ACKNOWLEDGEMENTS We acknowledge Hindustan Institute of Technology and Science for the financial assistance through HITS Seed Money Grant 2023 SEED/CRC/HITS/2022-23/0013. We owe a deep sense of gratitude to Prof. Dr. R. Jayavel, Former Dean, ACT campus and all the research scholars, Centre for Nanoscience and Technology, Anna University, Chennai for ensuring the facilities and instruments available in the laboratory.

FOR CITATION Abinaya K., Sharvanti P., N. Rajeswari Yogamalar Solution processed Ag–In–S nanoparticles as light adsorber in ZnO for photovoltaic application. *Nanosystems: Phys. Chem. Math.*, 2023, **14** (4), 454–466.

1. Introduction

Nanocrystals are increasingly gaining importance in modern technological advances due to their unique properties as well as the efforts to miniaturize the systems [1, 2]. In order to explore the novel physical properties and to realize the potential applications of these nanocrystals, the ability to fabricate and process nanocrystals are the first corner stone in nanotechnology [3, 4]. Silver sulphide (Ag₂S) is an important I–VI inorganic semiconductor material which finds diverse applications in energy devices [5, 6]. Ag₂S easily crystallizes in monoclinic phase and exhibits an anisotropic growth with controlled particle size. The Ag₂S in nano-sized structure appears to be a promising candidate in the conversion of the solar energy to the electrical energy as it has a narrow optical bandgap which can be tuned in the range of 1 eV to 2 eV. Tuning the bandgap and aligning the bandgap with the lattice matched hetero-structures play an important role in sensing and adsorbing the maximum available light energy (visible region and infra-red region) of the solar spectrum [7, 8]. Thus, the influence of above two parameters (nano-size confinement and optical bandgap engineering) on light harvesting is effectively investigated with the incorporation of high conductivity indium (In) metal ion by conventional wet chemical precipitation method into Ag₂S lattice. The major advantages of wet chemical method are relatively economical, large scale production, low energy consumption, and wide ranges of metals, metal oxides, metal sulphide, and nanocomposites are synthesized with peculiar morphology [9, 10]. The choice of In³⁺ metal ion, promotes more electron injections and with high ionic conductivity of $\sigma = 10^7 \Omega^{-1} \text{m}^{-1}$ enhances the electron transfer process and hence, reduces the electron-hole recombination process.

Mingxia J., et. al. reported the strong emitting photoluminescence properties of silver indium sulphide AgInS₂ quantum dots towards the power conversion efficiency (PCE) and long stability bio-imaging [11]. Highly luminescent AgInS nanoparticles are synthesized by Watcharaporn H., et. al. through two-step injection process [12]. Here, the AgInS

TABLE 1. The photovoltaic performance of Ag₂S, In₂S₃, and silver indium sulphide AgInS₂ as an adsorber and buffer layer in solar cell

Sample	Solar cell	Synthesis method	Photovoltaic Performance			Ref. No.
			V _{OC} (V)	J _{SC} (mAcm ⁻²)	η %	
Ag ₂ S as absorber layer	Inverted organic polymer solar cell	Spray pyrolysis Nano-particles	0.52	16.50	5.15	[15]
In ₂ S ₃ as buffer layer	CIGS	PVD Thin film	0.51	30.83	2.88	[16]
In ₂ S ₃ as electron transport layer	Perovskite solar cell	Solvent-thermal method Nanosheets	1.06	21.56	15.88	[17]
Cu diffused AgInS ₂	Heterojunction solar cell	Solution method Nano-powder	0.54	6.74	1.13	[18]
AgInS ₂ as electron transport layer	Perovskite solar cell	Solution method Nano-powder	1.12	22.20	13.8	[19]

core is coated with the gallium sulphide (GaS_x) shell and enhanced the photoluminescence quantum efficiency yield. The systematic characterization studies of graphene (Gr) incorporated indium sulphide nano film exhibited significant modifications in structural and opto-electronic properties especially in PV and photocatalyst applications [13]. A review article on tailored indium sulphide based solar materials for solar energy conversion and utilization is systematically summarized and its advancements are highlighted in detailed [14]. Mohammed Hamed S.G. employed silver sulphide nanoparticles as light trapping layer in an inverted solar cell [15]. The literary surveys on silver sulphide and indium sulphide for light harvesting are many in numbers. Despite these improvements, in this paper, an approach is made to integrate the properties of indium sulphide and silver sulphide into indium incorporated silver sulphide as light sensitizers / adsorbers in stable metal oxide ZnO based *pn* junction PV cell. To differentiate and to characterize the significance of the present work, Table 1 is tabulated to show the PV performance of individual chemical compounds Ag₂S, In₂S₃ and silver indium sulphide AgInS₂ acting as an adsorber or buffer layer in solar cell [15–19].

Here, a wet chemically synthesized Ag₂S and In incorporated Ag₂S are individually added with the ZnO nanorods to form the compound nanocomposites. The so-formed compound nanocomposites are deposited as *n*-type layer in heterojunction PVI and the efficiency of the assembled devices are compared, measured and evaluated by current density – voltage (*J-V*) characterization.

2. Experimental

2.1. Synthesis

The following reagents – silver nitrate AgNO₃, sulphur powder, sodium hydroxide pellets (NaOH), indium acetate In(CH₃COO)₃, poly-ethylene glycol (PEG), zinc nitrate ZnNO₃, cetrimide (CTAB), ammonia solution NH₃OH, were purchased from Merck with high purity and were used without further purifications.

In a typical synthesis of ZnO nanorods, 0.1 M of zinc nitrate was dissolved in 80 mL of deionized water (DW). To establish a controlled and anisotropic growth, 0.1 mM of capping agent namely PEG was added and stirred continuously for 30 min. A clear transparent solution was obtained implying the complete dissolution of crystal. Further, to initiate the precipitation process, 0.2 M of NaOH pellets were added and the transparent solution turned to milky white. Then, the solution mixture was transferred to hot air oven maintained at 90°C for 6 h and finally, the obtained solution was centrifuged repeatedly and vacuum dried at 60°C for 4 h to get crystallized white ZnO nanopowders (“Z”).

The pure and indium incorporated silver sulphide nanocomposites were prepared similarly. For Ag₂S synthesis, 0.2 M of silver nitrate and 0.2 mM of CTAB were dissolved in 50 mL of EG and pre-heated at 120°C for 30 min. Then a solution mixture of 0.6 M of sulphur powder and 1 M of NaOH pellets were dissolved in another 50 mL of EG and stirred for 30 min. Now, both the solutions were mixed and maintained at 120°C for 8 h in hot air oven. A black precipitate was obtained after centrifugation, vacuum dried at 60°C for 4 h and the sample was named as “AS”. The same methodology was adopted to synthesize indium incorporated Ag₂S nanocomposites, where 40 mM of indium acetate was added along with the silver precursor and the resulted sample powder was referred as “AIS”.

In the synthesis of compound nanocomposites by in-situ chemical precipitation method, the host material compound “Z” and the light sensitizer were taken in the ratio of 4:1 and were grown simultaneously. The as-synthesized “Z” was dispersed in 30 mL of EG, 10 mL of DW and 10 mL of methanol. The above solvent composition was mainly to promote

the adhesion of light sensitizer to the host compound and further, to establish controlled growth kinetics. Now, the as-synthesized "AS" and "AIS" were individually dispersed in the above solution mixture and maintained at 120°C for 8 h in hot air oven. The obtained precipitates were washed, centrifuged and vacuum dried. The as-synthesized nanocomposites were referred as "ZAS" and "ZAIS".

The entire procedures involved in the nanocomposites synthesis and the photograph of Z, AS, AIS, ZAS, and ZAIS were shown in the Fig. 1 and Fig. 2 respectively. In Fig. 2, the addition of In^{3+} metal ion precursor and the formation of nanocomposites resulted in a wide color variations from dirty white (Z) and black (AS) to dark grey (ZAS) and orange brown (AIS and ZAIS) solutions. The color variations might be due to the formation of different crystal structures or unusual optical properties which would be evaluated in the subsequent material characterizations.

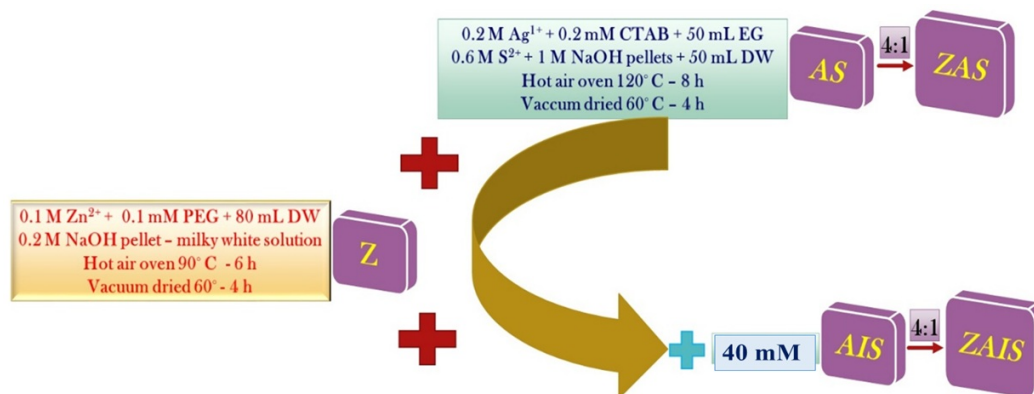


FIG. 1. The entire synthesis procedures of ZnO based compound nanocomposites by wet chemical method

2.2. Characterizations

The crystalline phases were verified with Mini Flex II Rigaku X-ray diffractometer (XRD) at a scanning rate of 0.2°/min in the range of 20° to 60° with Cu $K_{\alpha 1}$ radiation (1.5406Å) operated at 40 kV and 35 mA. The morphological study was carried out using TESCAN Vega III scanning electron microscopy (SEM) at an accelerating voltage of 5 kV to 10 kV. Room temperature UV-visible diffusion reflectance spectroscopy (DRS) data was acquired using T90+ UV/Vis spectrophotometer. Here, BaSO₄ powder was used as reference and the spectrum was recorded at room temperature in the wavelength range of 200 nm to 900 nm with the speed of 0.5 nm/s. The $J-V$ measurements for the device were measured using a Keithley sourcemeeter with 100 mW/cm² AM 1.5G of solar spectrum illumination.



FIG. 2. Photographic view of the as-synthesized samples Z, AS, AIS, ZAS and ZAIS nanocomposites

3. Results and discussions

3.1. Phase analysis

The Fig. 3 shows the typical XRD pattern of as-synthesized ZnO nanostructures (Z). All the diffraction peaks were referred with standard JCPDS database of 89-1397 and indexed as hexagonal phase wurtzite structure of ZnO. The absence of other secondary diffraction peaks indicates the phase purity of the as-synthesized ZnO nanostructure. The diffraction pattern consists of very narrow and sharp peaks, revealing the improved crystalline with ordered orientation of atoms in the

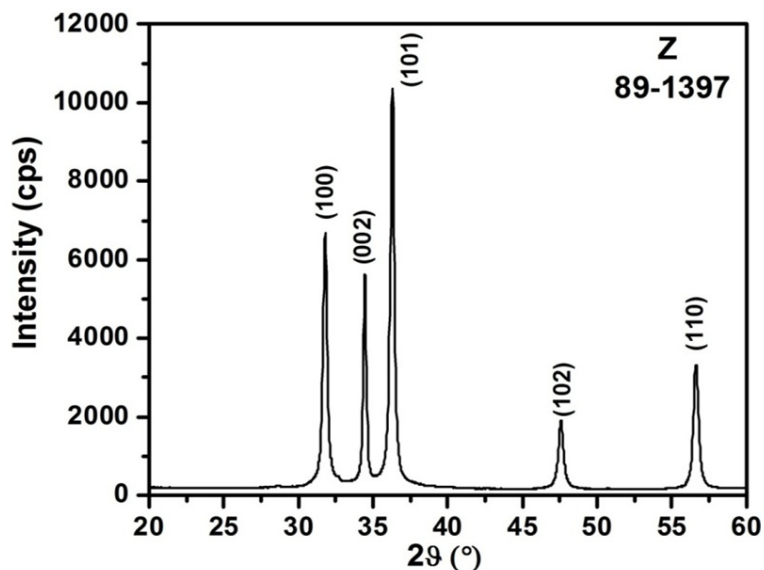


FIG. 3. The XRD pattern of PEG capped ZnO nanostructures (Z)

crystal lattice. For crystallite size analysis, the high intense (101) reflection of the hexagonal phase ZnO was employed. The average crystallite size d_{avg} was calculated from the instrumental corrected full width half maximum using Scherrer equation $d_{avg} = \left(\frac{0.9\lambda}{\beta \cos \theta} \right)$ and was found to be 47 nm for Z synthesized by the chemical precipitation method [20].

The XRD patterns of silver sulphide (AS) and transition metal indium incorporated silver sulphide (AIS) nanostructures were shown in the Fig. 4(a) and Fig. 4(b), respectively. All the diffraction peaks of AS were referred, matched

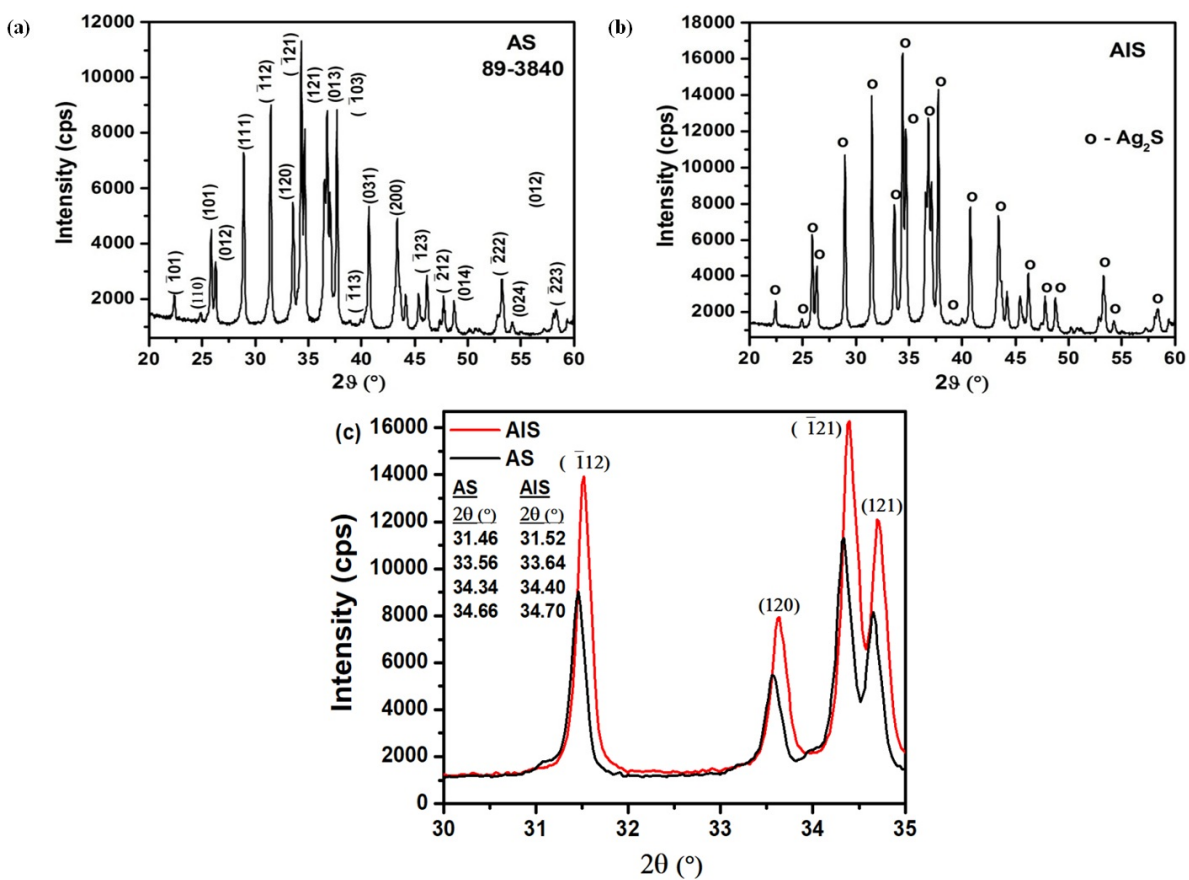


FIG. 4. The XRD patterns of (a) pure, (b) indium incorporated silver sulphide nanoparticles and (c) the peak shift

and indexed with the standard JCPDS data number 89-3840. Here, the sample crystallizes in monoclinic phase and the preferred growth orientation was along the (121) plane at 34° . The *AIS* sample as shown in Fig. 4(b) also exhibits the similar diffraction pattern with increased intensity and slightly broadened in comparison to *AS*. The peaks are matched and indicated by the symbol “o” in the Fig. 4(b). Here, the dominant diffraction peak was slightly shifted towards the higher scattering angle implying the presence of tensile strain originating from the incorporation of In^{3+} metal ion in the lattice site of Ag^+ ion. As the ionic radius of In^{3+} (81 pm) was smaller than the Ag^+ ion (126 pm), the diffraction peak shift was towards the greater angle from 34.34° to 34.40° . The In^{3+} ions were well incorporated in the parent lattice and forming a solid solution with no clear demarcation of secondary phase. The secondary phase of InS_2 might be hidden as they share the common diffraction angle like 26° – 27° , 38° – 39° and 52° – 54° . The calculated d_{avg} using Scherrer equation for *AS* and *AIS* samples were 38 nm and 34 nm, respectively.

However, in the preparation of the compound nanocomposites (*ZAS* and *ZAIS*) by in-situ chemical precipitation method, few variations were cited in comparison to the pure sample. In *ZAS* sample, the diffraction peaks corresponding to both the hexagonal phase ZnO and monoclinic phase Ag_2S were noticed and represented by the symbol “#” and “o”, respectively, in Fig. 5(a). Here, the Ag_2S nanoparticles formed a compound with the parent matrix material ZnO and, hence, a *ZAS* nanocomposite was formed with the second phase (monoclinic). As the composition of ZnO and Ag_2S was maintained as 4:1, the growth of ZnO nanostructures was predominant. In *ZAS* compound nanocomposites, the XRD peak intensity of (002) at $\theta = 34^\circ$ was amplified and heightened than (100) plane in comparison to the pure *Z* nanostructure. The observation might be attributed to the superposition of (002) plane of ZnO and (121) plane of Ag_2S nanostructures or due to the inclusion of Ag_2S nanoparticles the ZnO preferred to grow along the *c*-axis orientation which can be evaluated from SEM study.

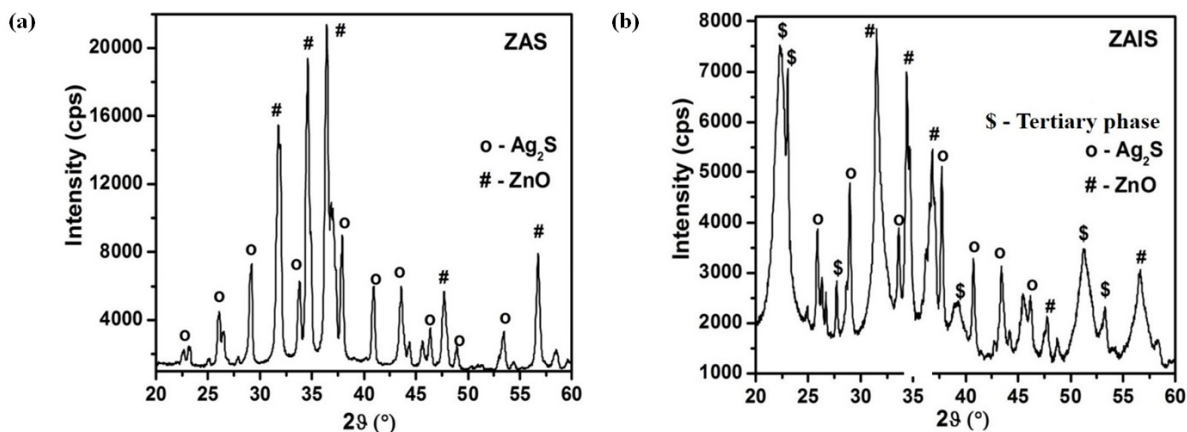


FIG. 5. The XRD patterns of (a) *ZAS* and (b) *ZAIS* compound nanocomposites synthesized by in-situ precipitation method

In *ZAIS* sample (Ref. Fig. 5(b)), apart from the crystal phases of ZnO and Ag_2S , a tertiary impurity peaks represented by the “\$” symbol, correspond to the indium hydroxide ($\text{In}(\text{OH})_3$) peaks (200) centered at 22.4° and (400) centered at 45.5° were referred and matched from the standard JCPDS data file number 73-1810 [21, 22]. Fig. 5(b) reflects that the diffraction peak intensities of hexagonal ZnO phase were highly suppressed and the growth was well pronounced along (100) plane due to the large distribution of small sized tertiary phase particles on ZnO lattice. The above reflections might be ascertained to the rapid nucleation and increased growth rate of tertiary phase in the prescribed synthesis condition. The tertiary phase particles were chemically well-reacted with the host material and strained their lattices to a greater extent. Moreover, the activation energy required for the growth of metal hydroxides $\text{In}(\text{OH})_3$ (≈ 840 meV) was usually lower than the metal oxide formation ZnO (≈ 1 eV) particles and hence, the impurity formation. The SEM studies might support the above establishments.

In both the compound nanocomposites *ZAS* and *ZAIS*, the ZnO was strained tensile due to the occupation of other phase materials. From Scherrer equation, a reduced d_{avg} was obtained for *ZAS* (22 nm) and *ZAIS* (16 nm) compound nanocomposites due to the pure and In^{3+} metal ion incorporated Ag_2S light sensitizers.

3.2. Particle size distribution

The particle size distribution was collected by MALVERN Zetasizer version 6 and for the measurement, the powder samples were suspended in the water solvent. Here, the *Z*, *AS*, *AIS*, *ZAS*, and *ZAIS* particles exhibited a wide size distribution as depicted in Fig. 6 ranging from 400 nm to $1.2 \mu\text{m}$. The wide particle size distributions were ascertained to the inclusion of nano-sized $\text{In}(\text{OH})_3$, Ag_2S and indium incorporated Ag_2S on the high crystalline ZnO nanostructures. Approximately 3% of InS_2 secondary phase is seen in the *AIS* sample which was not identified in the XRD (Ref. Fig. 4(b))

TABLE 2. The Z-average and particle size/phase distribution of Z, AS, AIS, ZAS, and ZAIS nanocomposites

Sample	Z-Average	Peak 1 – ZnO Phase	Peak 2 – Ag ₂ S Phase	Peak 3 – Impurity Phase
Z	1967	992 – 100%		
AS	582		367 – 100%	
AIS	466		522 – 97.10%	5049 – 2.90% (InS ₂)
ZAS	1144	2117 – 100%	Hump at 400 nm	
ZAIS	1202	1343 – 89.70%		5376 – 3.30% (InS ₂) 196 – 7.00% (In(OH) ₃)

due to the peak overlapping. In *ZAIS* compound nanocomposites, the particle distributions were referred in three different segments implying the formation of small percentage of tertiary phase impurities with reduced crystallite size. The Z-average, particle size and phase distribution of all samples are tabulated in Table 2.

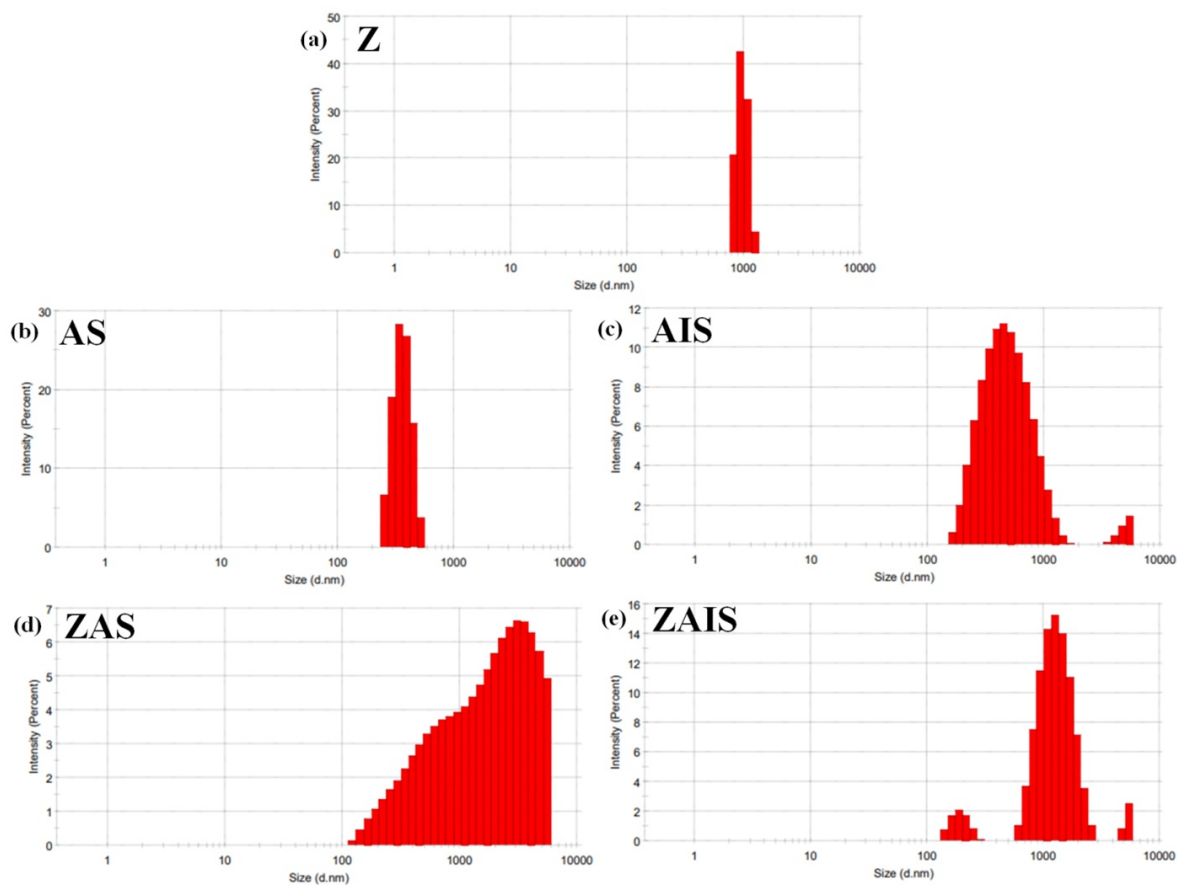


FIG. 6. The particle size distribution of Z, AS, AIS, ZAS, and ZAIS nanocomposites

3.3. Heat transfer mechanism

To evaluate the formation of secondary and tertiary phase impurities in the synthesized nanocomposites, the thermal decomposition study was performed by TG/DTA analysis where the samples were heated from room temperature to 800° at constant heating rate of 10°C/min in air and depicted in Fig. 7. All the samples exhibit similarity with host atom and dopant atom decomposition and the weight reduction is found to be low. While the maximum weight reduction of 29% is observed for the *ZAIS* due to the existence of residual phase materials present in the sample. Further, the occurrence of multistage decomposition beyond 400°C implies the process of crystallization and chemisorptions of intermediate molecules as inferred from the DTG curve. The DTG curve of *ZAIS* shows multiple sharp exothermic peaks revealing the thermal instability of as-synthesized samples.

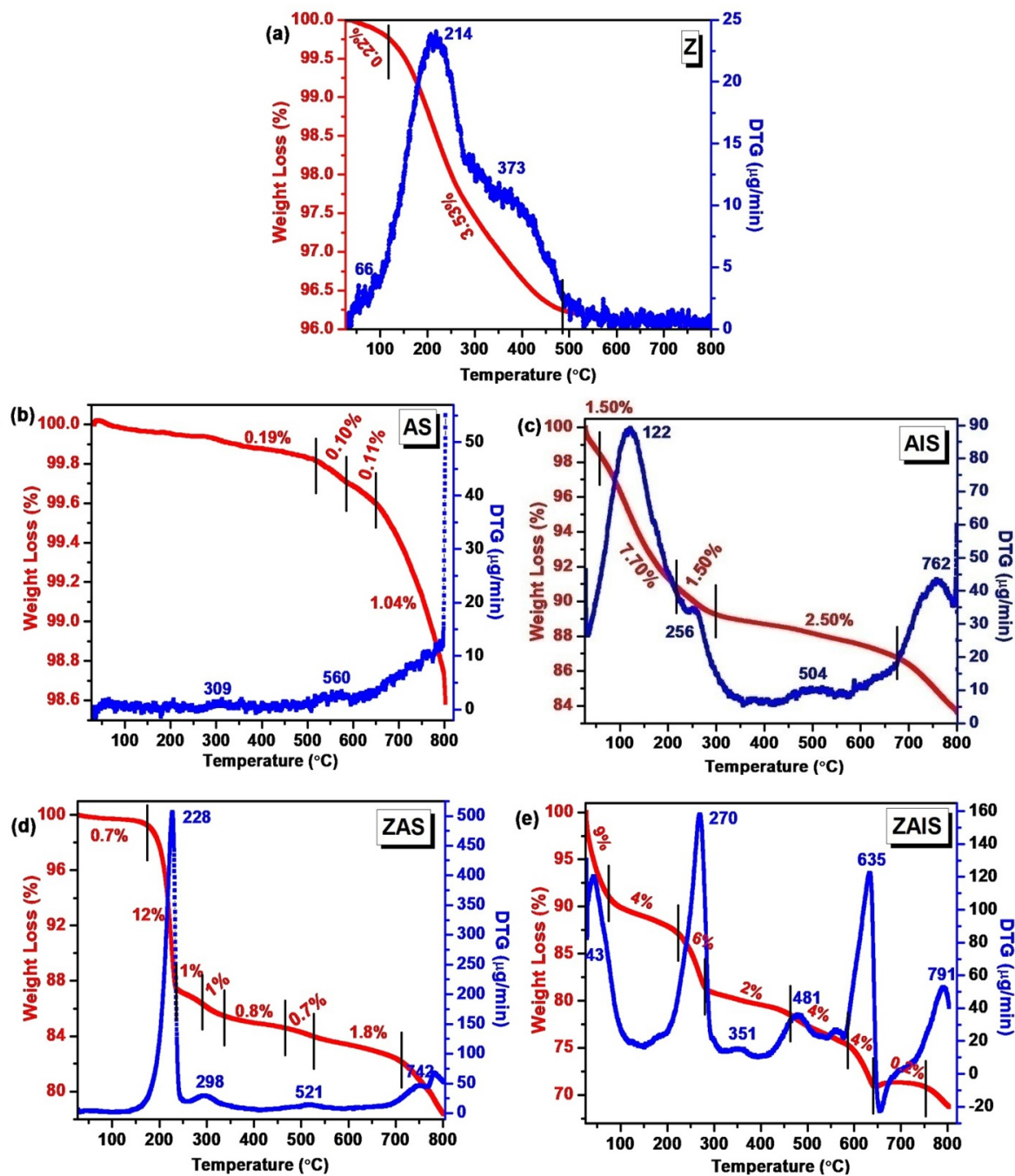


FIG. 7. The TG/DTG plot of (a) Z, (b) AS, (c) AIS, (d) ZAS, and (e) ZAIS nanocomposites

3.4. Morphological analysis

The typical SEM images of the ZnO nanoparticles were shown in Fig. 8(a) and Fig. 8(b). From the low and high magnified SEM micrographs, one can visualize the flower-like arrangement of ZnO nanostructures. Each petal of varying dimensions was assembled and architecture to form a flower-like arrangement. In high magnified SEM image shown in Fig. 8(b), the dimension of each petal was measured and was in the range of 400 nm to 720 nm. Few of the petals were immature and unable to form a complete flower-like structure. Here, the capping molecule PEG confine the growth and promote an anisotropic growth and, thus, resulting in unique morphology. The as-synthesized AS and AIS samples were nano-sized and non-homogeneous particle in nature and were displayed in Fig. 9 and Fig. 10. In Fig. 10(a-b), the nano-sized AS come closer to each other due to large surface area and forms an uneven oval, spherical and irregular structure. However, in Fig. 11(a-b), the degree of aggregation and agglomeration of AIS particles were higher than AS and, hence, distinct particle size and definite morphology cannot be assigned.

The SEM micrographs of ZAS and ZAIS compound nanocomposites synthesized by in-situ chemical precipitation method were portrayed in the Fig. 11 and Fig. 12, respectively. The image in Fig. 11(a) and in Fig. 12(a) clearly pictures

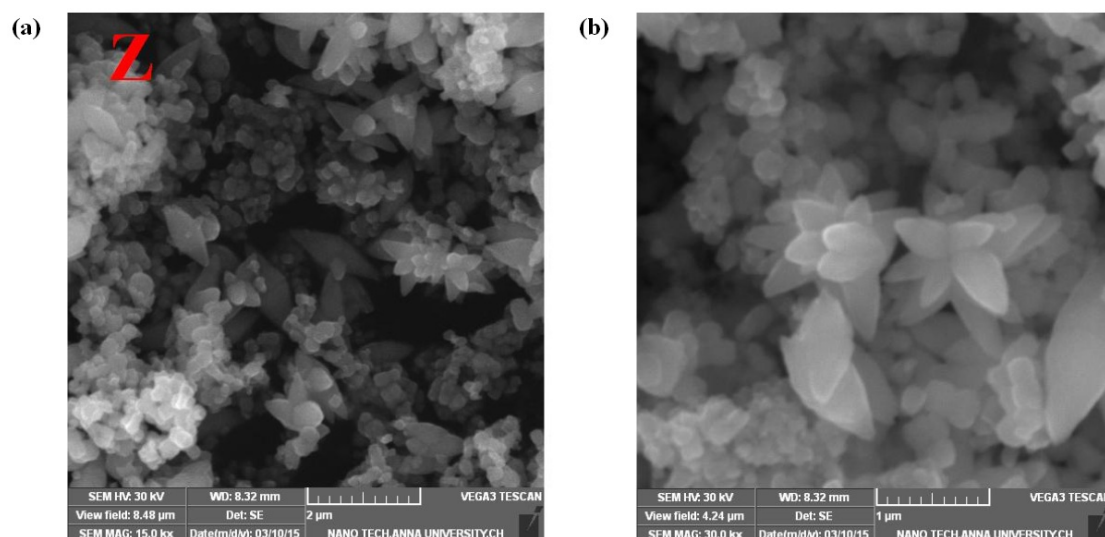


FIG. 8. (a) Low and (b) high magnified SEM micrographs of Z nanostructures

that the samples were composed of both particle and rod like structures implying the formation of blender mixtures. The rods were evolved from the ZnO nanostructures and particles were grown from the AS and AIS nanoparticles. A long solid ZnO nanorods were developed from flower-like ZnO nanostructure (Ref. Fig. 8(b)) and re-crystallized in *c*-axis as inferred from the XRD characterization depicted in the Fig. 5(a). The light sensitizer nano-sized AS particles occupy the ZnO surface, they hinder the multi-dimensional growth and promotes the 1D rod like structure. The AS particles were randomly distributed and aggregated certainly. However, the ZnO nanorods so formed in the ZAIS compound nanocomposites were shortened, flat and broken due to the Oswald ripening process and re-crystallization (Ref. Fig. 12(b)) [23]. As the activation energy of tertiary phase particles were dominant, the growth and formation of solid 1D ZnO nanorod were highly inhibited and, hence, broken, immature, crushed rods with reduced crystallite size d_{avg} were produced. The promptly nucleated nano-sized AIS particles densely adhere to the broken surface and get adsorb to the rod surface firmly and evenly than AS particles. Thus, an ordered flower-like arrangement was distorted during the formation of compound nanocomposites.

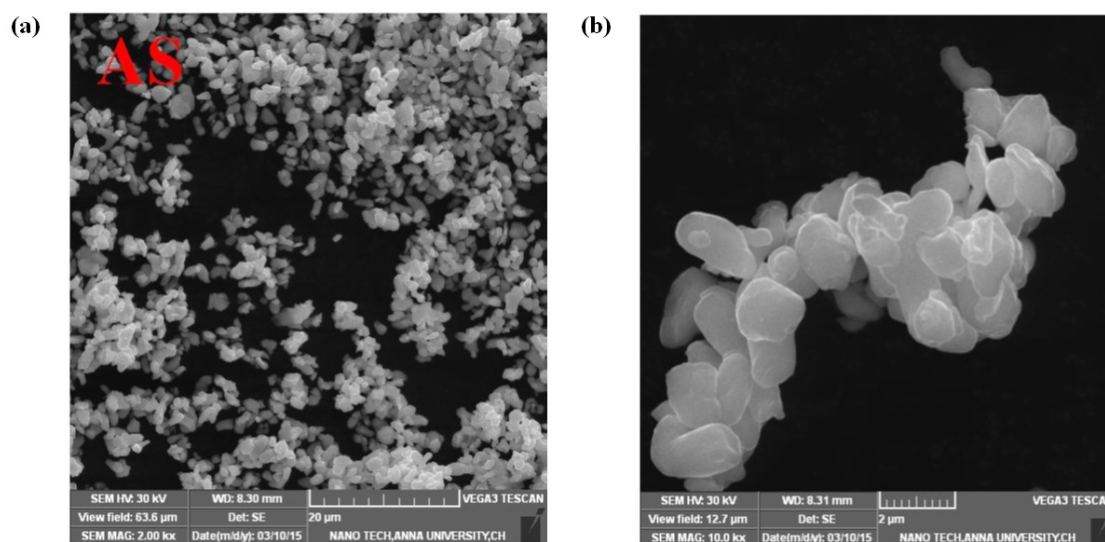


FIG. 9. (a) Low and (b) high magnified SEM micrographs of AS nanostructures

3.5. Diffuse Reflectance Spectroscopy

In adsorption study, room temperature UV-visible DRS spectra were recorded for the as-synthesized samples and were shown in Fig. 13. The ZnO nanostructures open a broad reflectance edge around 330 nm of wavelength. The nano-sized AS and AIS samples exhibit a narrowed reflectance with the onset of reflectance was found around 1220 nm. While

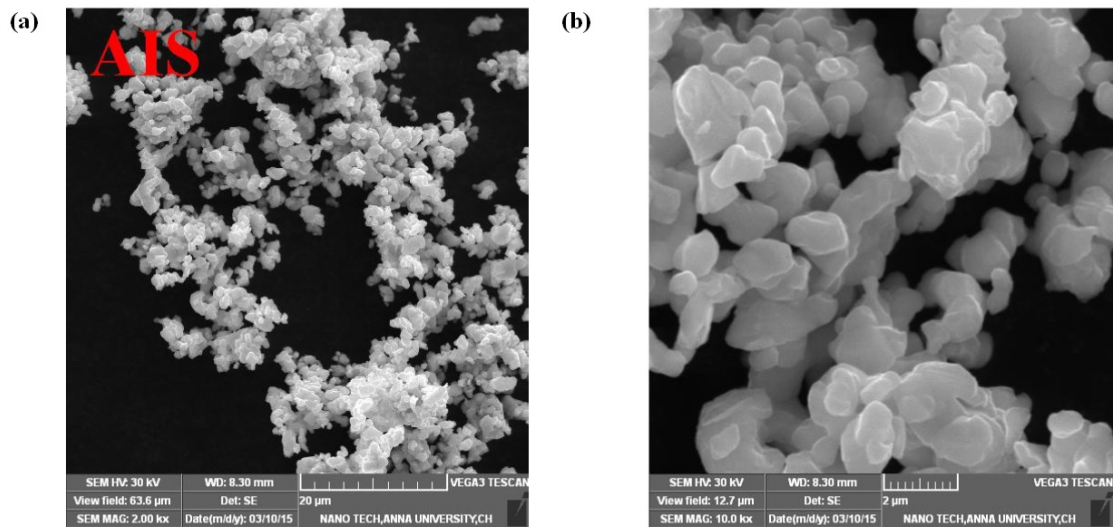


FIG. 10. (a) Low and (b) high magnified SEM micrographs of AIS nanostructures

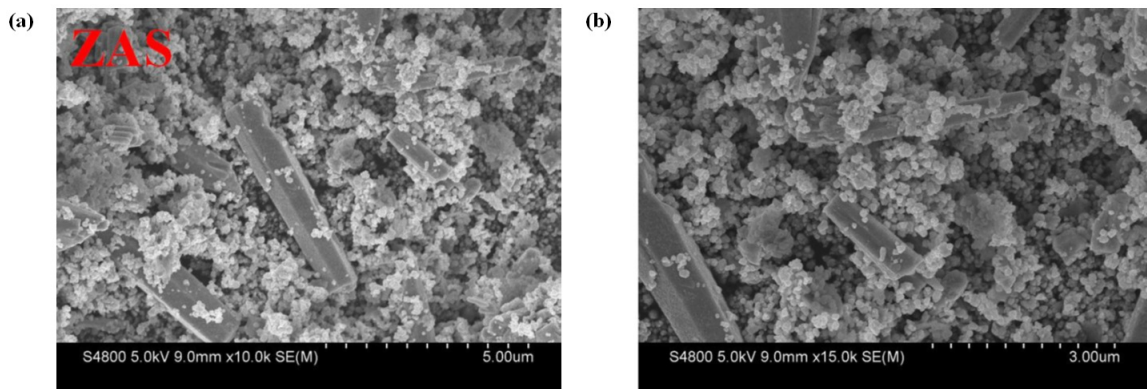


FIG. 11. (a) Low and (b) high magnified SEM micrographs of ZAS compound nanocomposites

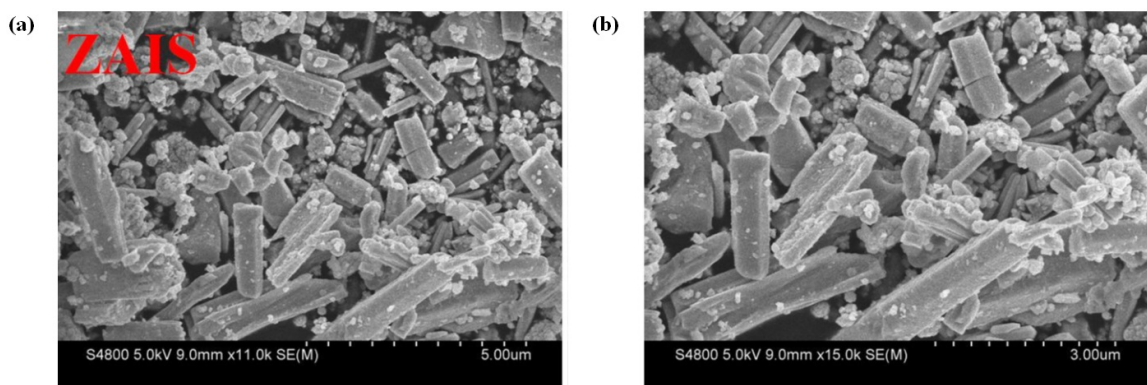


FIG. 12. (a) Low and (b) high magnified SEM micrographs of ZAIS compound nanocomposites

the compound nanocomposites, ZAS and ZAIS shows a reflectance commencing from 1100 nm. The sharp rise in the spectrum reveals the electronic band gap transition between the valence band and the conduction band.

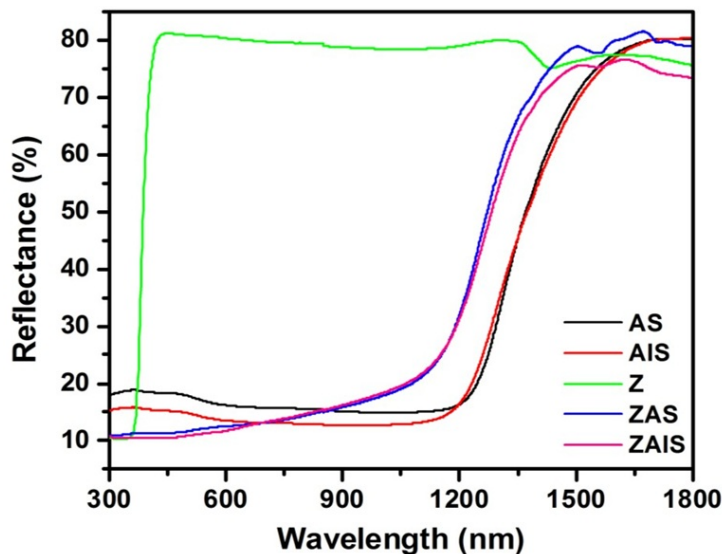


FIG. 13. The DRS spectra of Z, AS, AIS, ZAS and ZAIS nanocomposites

The optical band gap of the samples was derived from the Kubelka-Munk (K-M) function given by the equation $F(R_{\infty}) = \frac{(1 - R_{\infty})^2}{2R_{\infty}} = \frac{k(\lambda)}{s(\lambda)} = \alpha = \frac{(hv - E_g)^{1/2}}{hv}$. Here, $F(R_{\infty})$ is the K-M function, R_{∞} is the diffuse reflectance of an infinitely thick sample, $k(\lambda)$ is the absorption coefficient, $s(\lambda)$ is the scattering coefficient, and hv is the photon energy. The optical band gap E_g was obtained by extrapolating the linear portion of the curve plotted between $[F(R_{\infty})(hv)]^2$ and energy in eV [24]. For pure zinc oxide, the line is extrapolated and intersects at 3.16 eV as seen from Fig. 14(a). While AS and AIS samples exhibit an almost similar optical band gap of 0.82 eV implying that the dopant indium was properly substituted in the host lattice site silver sulphide (Ref. Fig. 14(b)). However, in ZAS and ZAIS, a linear extrapolation appears at 0.91 eV and further, an elemental rise appears around 2.5 to 3 eV involving the convoluted band gap of ZnO. Thus, in the compound nanocomposites, the optical bandgap occupies the intermediate position of Z and light sensitizers and, thus, covering the UV, visible and infra-red regions of solar spectrum. As a result, an optical bandgap tuning required for the photo-excitation of electrons can be accomplished with the ZAS and ZAIS sensitized by AS and AIS light sensitizers for solar cell applications.

4. Photovoltaic cell

The influence of light sensitizers AS and AIS in ZnO and the device performance were evaluated by the density-voltage (J - V) characteristics obtained using Keithley sourcemeter with 100 mW cm^{-2} AM 1.5 G solar illumination. The

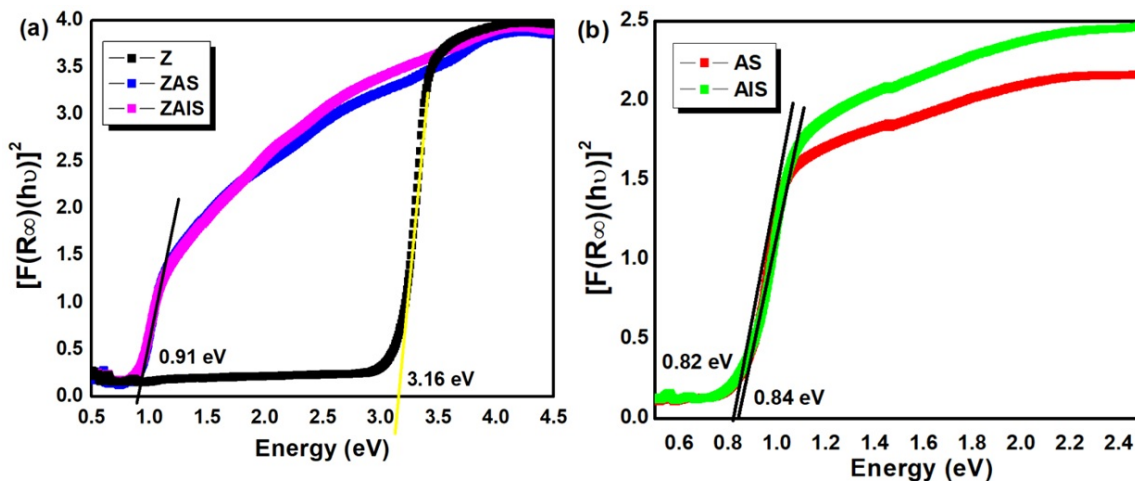


FIG. 14. Energy bandgap of as-synthesized (a) Z, ZAS, ZAIS nanocomposites and (b) AS, AIS samples

PV cell parameters of the devices, including the J_{sc} , V_{oc} , and FF values were calculated. In assembling the PV cell, sol-gel processed spin coating and successive ionic layer adsorption and reaction (SILAR) method were adopted for the film growth as prescribed in our earlier work [25]. To evaluate the role of light sensitizers and the In^{3+} metal ion, two different combinations of pn -junction based PV cells were designed. The first device composed of ZAS and the second with the ZAIS as n -type layer and Rose Bengal (RB) as p -type layer. Both the layers were successively spin coated on the ITO coated glass substrate. Finally, a proper Ohmic contact was established on the n -type material and p -type material by the selective etching of ITO substrate and DC sputtering of Au electrode respectively. The schematic model of PV device architecture and the device performance for ZAIS was illustrated in Fig. 15. An interface is formed between the RB and ZnO based nanocomposites. When solar light energy was absorbed by the junction, free charge carriers were generated and transported by means of driving force due to in-built electric field. The presence of nano-sized light sensitizers and the energy band matching of RB and nanocomposites, promoted more photons adsorption and transportation and thereby, inducing more current flows.

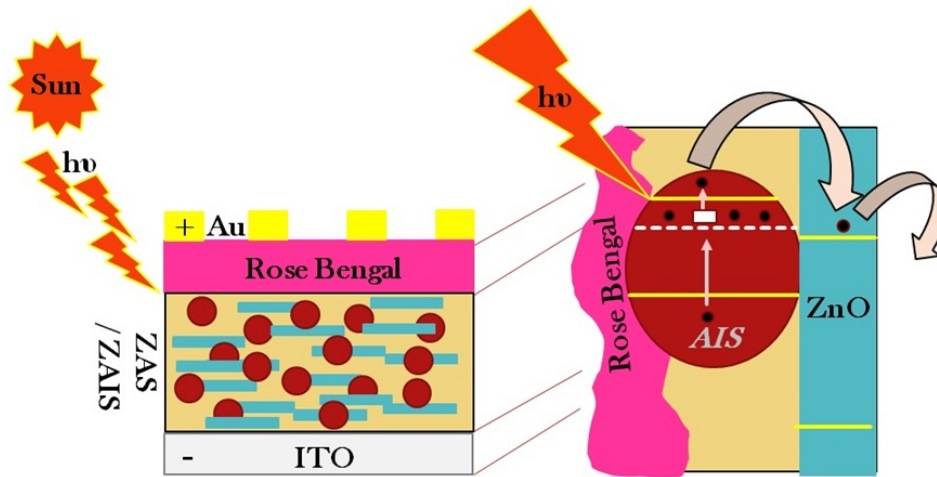


FIG. 15. The schematic model of photovoltaic device and working of ZAIS composed pn junction PV cell

The coating thickness of the hetero-layer (p -layer and n -layer) was visualized and measured from the cross-section SEM images of the ITO coated glass substrate as portrayed in Fig. 16(a) and Fig. 16(b). The chemical coating process resulted in dense overlapped coating with the thickness approaching $120 \mu\text{m}$ and the individual layer was not recognized.

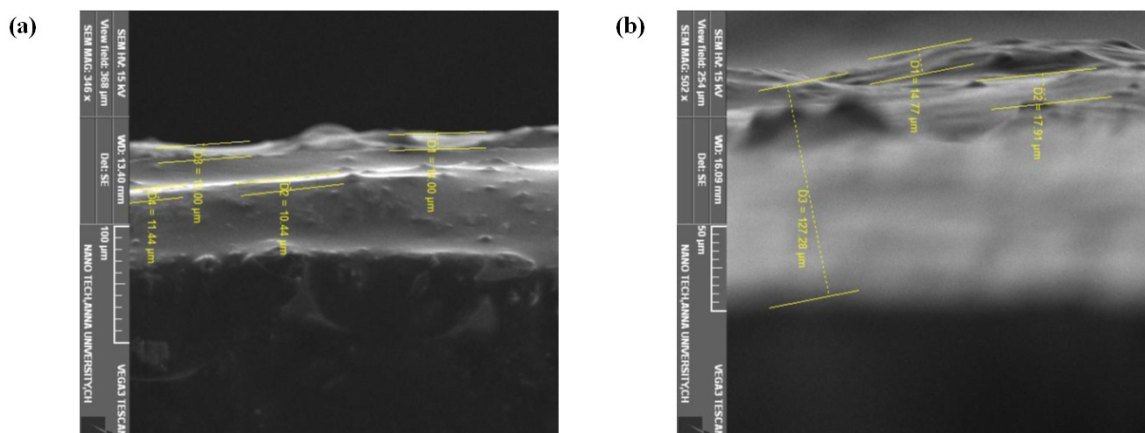


FIG. 16. The (a) cross-sectional images and (b) the approximate thickness measurement of assembled PV cell

4.1. J-V characteristics

The PV cell composed of ZAIS exhibited a higher efficiency of 1.2% evaluated against ZAS of 0.76% as revealed from Fig. 17(a) and Fig. 17(b). For the PV device applications, the pn -junction should promote facile charge transport which can be achieved by the incorporation of transition metal dopant In^{3+} ions.

In comparison with ZAS, the obtained results in ZAIS nanocomposites can be addressed by the following causes. In ZAIS, the structure of ZnO was strained and modified by the inclusion of indium incorporated Ag_2S nanoparticles which

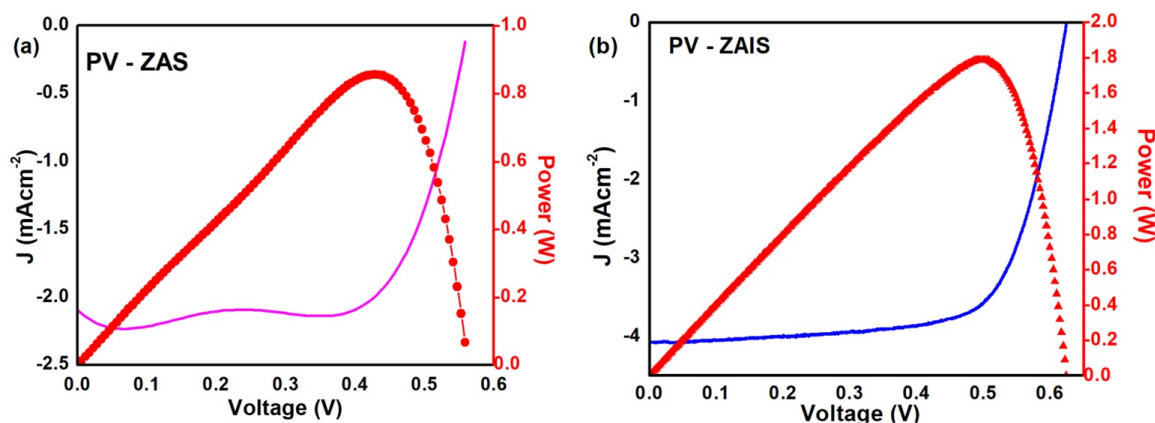


FIG. 17. Current density and voltage characteristics and power calculation of PV cells composed of (a) ZAS and (b) ZAIS compound nanocomposites

TABLE 3. Solar cell parameters of ZAS and ZAIS composed *pn* junction PV devices

PV devices	V_{OC} (V)	J_{SC} (mA/cm ²)	FF %	η (no unit)
RB / ZAS	0.56	2.70	50.00	0.76
RB / ZAIS	0.62	4.00	50.00	1.20

resides either at the lattice sites or on the surface of ZnO and, therefore, leads to the formation of defects (tertiary phase impurities). The strained region of ZnO lattice exhibits higher chemical reactivity and consequently easy displacement of electron density from the lattice plane. This surface alteration and intact adherence of nano-sized indium incorporated Ag₂S nanoparticles on the ZnO surface render facile and rapid charge transfer within the device. In addition, the size quantized AIS nanoparticles with optical band gap of 0.91 eV was included to absorb wide range of the solar spectrum and the nanoscale mixing of AIS nanoparticles into the ZnO matrix increased the interfacial area and promoted large number of excitons per incident photon. The above factors, thus, simultaneously control the J_{sc} , V_{oc} , and η parameters of the PV device.

Table 3 summarizes the PV cell parameters obtained for the two devices. From the table, the high V_{OC} and J_{SC} values were mainly due to the incorporation of In³⁺ metal ion with excess electrons and high conductivity respectively. The In³⁺ ions occupy beneath the conduction band of Ag₂S, donating the free electrons with low energy absorption and simultaneously transferring the excited electrons to the stable metal oxide ZnO due to its high conductivity. By this process, long lived more number of free electrons are transferred between the material compounds and, thus, increasing the current density J value from 2.7 mA/cm² in ZAS to 4.0 mA/cm² in ZAIS nanocomposites.

Though the choice of materials adopted for PV cell designing were preferable, the calculated efficiency was still not appreciable and the cause might be due to the tertiary phase impurities resulting in higher series resistance existing in the junction. The current-voltage I - V equation for the *pn* junction is given by $V_{OC} = \frac{k_B T}{e} \ln \frac{I_{ph}}{I_{sO}}$ [26]. In single junction ZAIS PV cell, the low efficiency was attributed to the defect induced recombination loss due to the existence of tertiary phase material. In addition, the thermalization loss further suppress the efficiency as residual intermediate phase materials were present which was evident from the TGA/DTA curve. In future work, an optimized synthesis method will be followed to furnish the higher efficiency.

5. Conclusions

In summary, we have established a simple wet chemical process nano-sized Ag₂S and In³⁺ metal ion incorporated Ag₂S method to enhance the light adsorption and light energy conversion for PV application. The improvement was attributed to the maximum light absorption in the visible and infra-red regions of the solar spectrum offered by the low optical bandgap Ag₂S and facile charge transport which arises from the high conductive indium metal ion in Ag₂S nanoparticles along with the 1D ZnO nanorods. The present work initiates the advantage of nano-sized AS and AIS inclusion in ZnO for PV application and with the proper device organization it would paves the way towards the high efficient PV cell.

References

- [1] Ahmet Z.S., Mohammed Ayaz U., Bekir S.Y., Abdullah A.S. Performance enhancement of solar energy systems using nanofluids: An updated review. *Renew. Energy*, 2020, **145**, P. 1126–1148.
- [2] Selvakumar P., Muthukumarasamy N., Agilan S., Vijayshankar A., Akila Y., Venkatraman M.R., Senthilarasu S., Dhayalan V. A review on the classification of organic / inorganic / carbonaceous hole transporting materials for perovskite solar cell application. *Arab. J. Chem.*, 2020, **13**, P. 2526–2557.
- [3] Zahra S. Recent progress in development of diverse kinds of hole transport materials for the perovskite solar cells: A review. *Renew. Sust. Energy Rev.*, 2020, **119**, P. 109608–109646.
- [4] Zinab H.B., Qamar W., Azhar F., Lukas Schmidt M., Thomas M., Rajan J. Advances in hole transport materials engineering for stable and efficient perovskite solar cells. *NanoEnergy*, 2017, **34**, P. 271–305.
- [5] Ambalika S., Rahul S., Nishat B., Asha Kumari. Review on synthesis, characterization and applications of silver sulphide quantum dots. *J. Mat. Sci. Res. Rev.*, 2021, **7**(3), P. 42–58.
- [6] Anjana V.N., Majo J., Sijo F., Alex J., Ebey P. Koshy, Beena M. Microwave assisted green synthesis of silver nanoparticles for optical, catalytic, biological and electrochemical applications. *Artif. Cells Nanomed. Biotechnol.*, 2021, **49**, P. 438–449.
- [7] Auttasit T., Kun-Lun W., Hao-Yu T., Ming-Way L., Gou Jen W. Ag₂S quantum dot-sensitized solar cells. *Electrochem. Commun.*, 2010, **12**, P. 1158–1160.
- [8] Nurul Syafiqah M., Suhaila S., Norasikin Ahmad L., Asri Mat Teridi M., Adib Ibrahim M. Effect of silver sulphide (Ag₂S) layer towards the performance of copper indium sulphide (CuInS₂) quantum dots sensitized solar cell. *Int. J. Nanotechnol.*, 2021, **17**, P. 795–806.
- [9] Hanlin H., Mriganka S., Xuejuan W., Jiaoning T., Chih-Wei C., Gang L. Nucleation and crystal growth control for scalable solution-processed organic–inorganic hybrid perovskite solar cells. *J. Mater. Chem. A*, 2020, **8**, P. 1578–1603.
- [10] Yaokang Z., Sze-Wing N., Xi L., Zijian Z. Solution-processed transparent electrodes for emerging thin-film solar cells. *Chem. Rev.*, 2020, **120**, P. 2049–2122.
- [11] Mingxia J., Yun L., Chenxi L., Hao B., Liting G., Peng C., Xiliang L. Strongly emitting and long-lived silver indium sulphide quantum dots for bioimaging: Insight into co-ligand effect on enhanced photoluminescence. *J. Colloid Interface Sci.*, 2020, **565**, P. 35–42.
- [12] Taro U., Kazutaka W., Dharmendar Kumar S., Shuzo H., Takahisa Y., Tatsuya K., Martin V., Tsukasa T., Susumu K. Narrow band-edge photoluminescence from AgInS₂ semiconductor nanoparticles by the formation of amorphous III–VI semiconductor shells. *NPG Asia Mater.*, 2018, **10**, P. 713–726.
- [13] Jilu C.J., Tina S., Sunny M., Shaji S., Augustine S. Investigations on the properties of indium sulphide – Graphene nanocomposites thin films. *Thin Solid Films*, 2020, **695**, P. 137758–137772.
- [14] Jingjing Z., Hou W., Xingzhong Y., Guangming Z., Wenguang Tu Sibow. Tailored indium sulphide-based materials for solar-energy conversion and utilization. *J. Photoch. Photobio. C: Photochem. Rev.*, 2019, **38**, P. 1–26.
- [15] Mohammed Hamed S.G., Michael A.A., Yong Z., Genene Tessema M. Silver sulphide nano-particles enhanced photo-current in polymer solar cells. *Appl. Phys. A*, 2020, **126**, P. 207–214.
- [16] Mohammad Istiaque H. Prospects of CZTS solar cells from the perspective of material properties, fabrication methods and current research challenges. *Chalcogenide Lett.*, 2012, **9**, P. 231–242.
- [17] Zhe X., Jihuai W., Yuqian Y., Zhang L., Jianming L. High-efficiency planar hybrid perovskite solar cells using indium sulphide as electron transport layer. *ACS Appl. Energy Mater.*, 2018, **1**, P. 4050–4056.
- [18] Asim G., Amlan J. Pal. Copper-diffused AgInS₂ ternary nanocrystals in hybrid bulk-heterojunction solar cells: Near-infrared active nanophotovoltaics. *Appl. Mater. Interfaces*, 2013, **5**, P. 4181–4189.
- [19] Anusit K., Pisist K., Takashi S. Silver-indium-sulphide quantum dots in titanium dioxide as electron transport layer for highly efficient and stable perovskite solar cells. *J. Mater. Sci.: Mater. Electron.*, 2019, **30**, P. 4041–4055.
- [20] Dan H., Peng S., Huihui Z., Huihui Y., Qi X., Zhongxi Y., Qi W. Flower-like In₂O₃ hierarchical nanostructures: synthesis, characterization, and gas sensing properties. *RSC Adv.*, 2014, **4**, P. 50241–50248.
- [21] Jiayong G., Xihong L., Jingheng W., Shilei X., Teng Z., Minghao Y., Zishou Z., Yanchao M., Shing Chi Ian W., Yong S., Yexiang T. Oxygen vacancies promoting photoelectrochemical performance of In₂O₃ nanocubes. *Sci. Rep.*, 2013, **3**, P. 1–7.
- [22] Mingxia J., Yun L., Chenxi L., Hao B., Liting G., Peng C., Xiliang L. Strongly emitting and long-lived silver indium sulphide quantum dots for bioimaging: Insight into co-ligand effect on enhanced photoluminescence. *J. Colloid Interface Sci.*, 2020, **565**, P. 35–42.
- [23] Yuqiang Y., Jihuai W., Xiaobing W., Qiyao G., Xuping L., Weihai S., Yuelin W., Yunfang H., Zhang L., Miaoliang H., Jianming L., Hongwei C., Zhanhua W. Suppressing vacancy defects and grain boundaries via Oswald ripening for high-performance and stable perovskite solar cells. *Adv. Mater.*, 2020, **32**, P. 1904347.
- [24] Dhanabal R., Chithambararaj A., Velmathi S., Chandra Bose A. Visible light driven degradation of methylene blue dye using Ag₃PO₄. *J. Environ. Chem. Engg.*, 2015, **3**, P. 1872–1881.
- [25] Rajeswari Yogamalar N., Sadhanandam K., Chandra Bose A., Jayavel R. Quantum confined CdS inclusion in graphene oxide for improved electrical conductivity and facile charge transfer in hetero-junction solar cell. *RSC Adv.*, 2015, **5**, P. 16856–16869.
- [26] Markus D., Thathit S., Arif H., Ahmad T., Abdulloh F., Risa S. Shockley's equation fit analyses for solar cell parameters from I–V curves. *Int. J. Photoenergy*, 2018, **2018**, P. 1–7.

Submitted 27 September 2022; revised 17 March 2023; accepted 11 June 2023

Information about the authors:

K. Abinaya – Doctoral Researcher, London South Bank University, London SE1 0AA, UK

P. Sharvanti – Senior Process Engineer, Research and Development, Saint Gobain, San Diego, California 92123, USA

N. Rajeswari Yogamalar – Department of Physics, Hindustan Institute of Technology and Science, Padur, Kelambakkam, Chennai – 603103, India; ORCID 0000-0002-4954-6552; rajeswariyogamalar.n@gmail.com

Conflict of interest: the authors declare no conflict of interest.